

Atom-atom interactions around the band edge of a photonic crystal waveguide

J. D. Hood^{1,2}, A. Goban^{1,2,†}, A. Asenjo-Garcia^{1,2}, M. Lu^{1,2}, S.-P. Yu^{1,2}, D. E. Chang³, and H. J. Kimble^{1,2,*}

¹ *Norman Bridge Laboratory of Physics MC12-33*

² *Institute for Quantum Information and Matter,
California Institute of Technology, Pasadena, CA 91125, USA and*

³ *ICFO-Institut de Ciències Fotoniques, The Barcelona Institute
of Science and Technology, 08860 Castelldefels (Barcelona), Spain*

(Dated: December 12, 2022)

Tailoring the interactions between quantum emitters and single photons constitutes one of the cornerstones of quantum optics. Coupling a quantum emitter to the band edge of a photonic crystal waveguide (PCW) provides a unique platform for tuning these interactions. In particular, the crossover from propagating fields $E(x) \propto e^{\pm ik_x x}$ outside the bandgap to localized fields $E(x) \propto e^{-\kappa_x |x|}$ within the bandgap should be accompanied by a transition from largely dissipative atom-atom interactions to a regime where dispersive atom-atom interactions are dominant. Here, we experimentally observe this transition for the first time by shifting the band edge frequency of the PCW relative to the D₁ line of atomic cesium for $\bar{N} = 3.0 \pm 0.5$ atoms trapped along the PCW. Our results are the initial demonstration of this new paradigm for coherent atom-atom interactions with low dissipation into the guided mode.

PACS numbers: 42.50.Ct, 42.50.Nn, 37.10.Gh, 42.70.Qs

Recent years have witnessed a spark of interest in combining atoms and other quantum emitters with photonic nanostructures [1]. Many efforts have focused on enhancing emission into preferred electromagnetic modes relative to vacuum emission, thereby establishing efficient quantum atom-light interfaces and enabling diverse protocols in quantum information processing [2]. Photonic structures developed for this purpose include high-quality cavities [3–7], dielectric fibers [8–13], and metallic waveguides [14–16]. Photonic crystal waveguides (PCWs) are of particular interest since the periodicity of the dielectric structure drastically modifies the field propagation, yielding a set of Bloch bands for the guided modes [17]. For example, recent experiments have demonstrated superradiant atomic emission due to a reduction in group velocity for an atomic frequency near a band edge of a PCW [18].

A quite different paradigm for atom-light interactions in photonic crystals was proposed in Refs. [19–22], but has yet to be experimentally explored. In particular, when an atomic transition frequency is situated within a bandgap of a PCW, an atom can no longer emit propagating waves into guided modes (GMs) of the structure. However, an evanescent wave surrounding the atoms can still form, resulting in the formation of a stable atom-photon bound state. This phenomenon has attracted new interest recently as a means to realize dispersive interactions between atoms without dissipative decay into GMs. The spatial range of atom-atom interactions is

tunable for 1D and 2D PCWs and set by the size of the photonic component of the bound state [23, 24]. Many-body physics with large spin exchange energies and low dissipation can thereby be realized, in a generalization of cavity QED arrays [25, 26]. Fueled by such perspectives, there have been recent experimental observations with atoms [18, 27, 28] and quantum dots [29, 30] interacting through the GMs of photonic crystal waveguides, albeit in frequency regions outside the bandgap, where GMs are propagating fields.

In this manuscript, we report the first observation of a collective dispersive shift of the atomic resonance frequency due to atom-atom interactions around the band edge of a photonic crystal. Thermal tuning allows us to control the offset of the band edge frequency (ν_{BE}) of the PCW relative to frequency ν_{D1} of the D₁ line of cesium. In both the dispersive domain (i.e., ν_{D1} outside the bandgap with electric field $E(x) \propto e^{\pm ik_x x}$) and reactive regime (i.e., ν_{D1} inside the bandgap with $E(x) \propto e^{-\kappa_x |x|}$), we record transmission spectra for atoms trapped along the PCW, as illustrated in Fig. 1(a).

To connect the features of the measured transmission spectra to underlying atom-atom radiative interactions, we have developed a formalism based on the electromagnetic Green’s function. The model allows us to infer the peak single-atom frequency shift, $J_{\text{1D}}(\Delta_{\text{BE}})$, and decay rate to the guided mode, $\Gamma_{\text{1D}}(\Delta_{\text{BE}})$. These quantities depend on the detuning $\Delta_{\text{BE}} = \nu_{\text{D1}} - \nu_{\text{BE}}$ between the atomic ν_{D1} and band edge ν_{BE} frequencies. From decay-rate measurements, we infer the average number of trapped atoms to be $\bar{N} = 3.0 \pm 0.5$. Due to the exponential localization of the field in the bandgap, we measure a ratio $\mathcal{R} = \Gamma_{\text{1D}}/J_{\text{1D}} = 0.05 \pm 0.17$ at $\Delta_{\text{BE}} = 50$ GHz. For comparison, the analogous ratio of dissipative to coherent rates predicted from conventional cavity quantum

[†] Present address: JILA, University of Colorado, 440 UCB, Boulder, Colorado 80309, USA

* hjkimble@caltech.edu

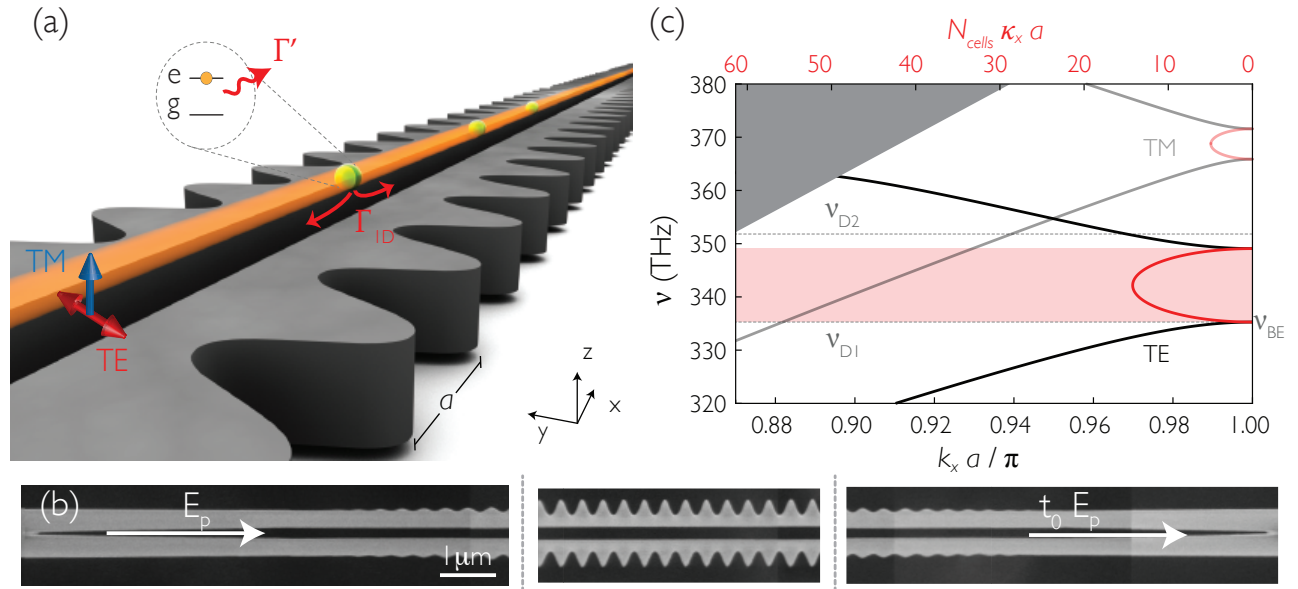


FIG. 1: Description of the alligator photonic crystal waveguide (APCW). **(a)** Atoms are trapped above the APCW. The orange cylinder represents the region of optical confinement by a dipole-force optical trap in which atoms are localized approximately 125 nm above the surface of the APCW and tightly confined in the y, z directions transverse to the central x -axis of the device [18]. The three green spheres represent trapped atoms that interact radiatively via the fundamental TE guided mode, polarized mainly along y . The decay rate for a single atom into the APCW is Γ_{ID} (red arrows), and the decay rate into all other modes is Γ' (wavy red). **(b)** SEM images of portions of the tapering and APCW sections. The suspended silicon nitride device (grey) consists of 150 cells and 30 tapering cells on each side. The lattice constant is $a = 370$ nm and thickness is 185 nm. **(c)** Calculated band structure of the fundamental TE (solid) and TM (translucent) modes using an eigenmode solver [32] and the measured SEM dimensions, which are modified within their uncertainty to match the measured bands. The black curves represent the Bloch wave-vector k_x (lower axis). The red curves show the attenuation coefficient κ_x of the field for frequencies in the bandgap (upper axis), and are calculated by means of an analytical model [33]. The dotted lines mark the frequencies of the Cs D_1 ($\nu_{D1} = 335.1$ THz) and D_2 ($\nu_{D2} = 351.7$ THz) transitions. The dielectric band edge is indicated as ν_{BE} . The pink (gray) shaded area represents the TE bandgap (the light cone).

electrodynamics (cQED) is $\mathcal{R}_{cQED} = 0.30 \pm 0.04$ for a cavity with similar parameters to our PCW [31].

Alligator Photonic Crystal Waveguide - Figure 1(a) provides an overview of our experiment with atoms trapped near and strongly interacting with the TE-like mode of an alligator PCW (APCW). The suspended silicon nitride structure consists of $N_{\text{cells}} = 150$ nominally identical unit cells of lattice constant $a = 370$ nm, and is terminated by 30 tapering cells on each side, as shown in the SEM images in Fig. 1(b). The tapers mode-match the fields of the APCW to the fields of uncorrugated nanobeams for efficient input and output coupling. Design, fabrication, and characterization details are described in Refs. [18, 27, 28]. Figure 1(c) shows the nominal cell dispersion relations for the TE (polarized mainly along y) and TM-like modes (polarized mainly along z). After release of the SiN structure from the Si substrate, a low power CF_4 etch is used to align the lower/'dielectric' TE band edge (ν_{BE}) to the Cs D_1 transition (ν_{D1}). The TM mode has band edges far detuned from the both the Cs D_1 and D_2 lines. In our experiment, the TE mode is used to probe the atoms, while the TM mode with approximately linear dispersion serves to calibrate the density and trap properties.

In order to better understand atomic interactions with the APCW, it is helpful to visualize the spatial profile of the fields generated absent atoms, when light is input from one end. Figure 2(a) shows the measured intensity along the length of the APCW as a function of probe detuning $\delta_{BE} = \nu_p - \nu_{BE}$ around the band edge, where ν_p is the probe frequency. The intensity was measured by imaging weak scatterers along the length of the APCW that, after calibration, serve as local probes of the intensity [33]. Figure 2(b) shows the corresponding FDTD simulated intensity [34]. In both images, resonances appear at $\nu_p = \nu_{1,2,3}$ due to the weak cavity formed by the reflections of the tapers. These resonances can be understood from the fact that the effective wave-vector near the band edge is given by $\delta k_x = \pi/a - k_x$ for $\Delta_{BE} < 0$, and the n 'th resonance at frequency ν_n is such that $\delta k_x = n\pi/L$, where L is the effective length of the APCW (including field penetration into the tapers). Fig. 2(c) shows a plot of $|E(x)|^2$ for a probe input at frequency $\nu_p = \nu_1$ at the first resonance. Inside the bandgap ($\Delta_{BE} > 0$) the field is evanescent, and $\delta k_x = i\kappa_x$. Fig. 2(d) plots $|E(x)|^2$ for probe frequency $\nu_p = \nu_{BG}$ inside the bandgap, and shows the exponential decay of the intensity.

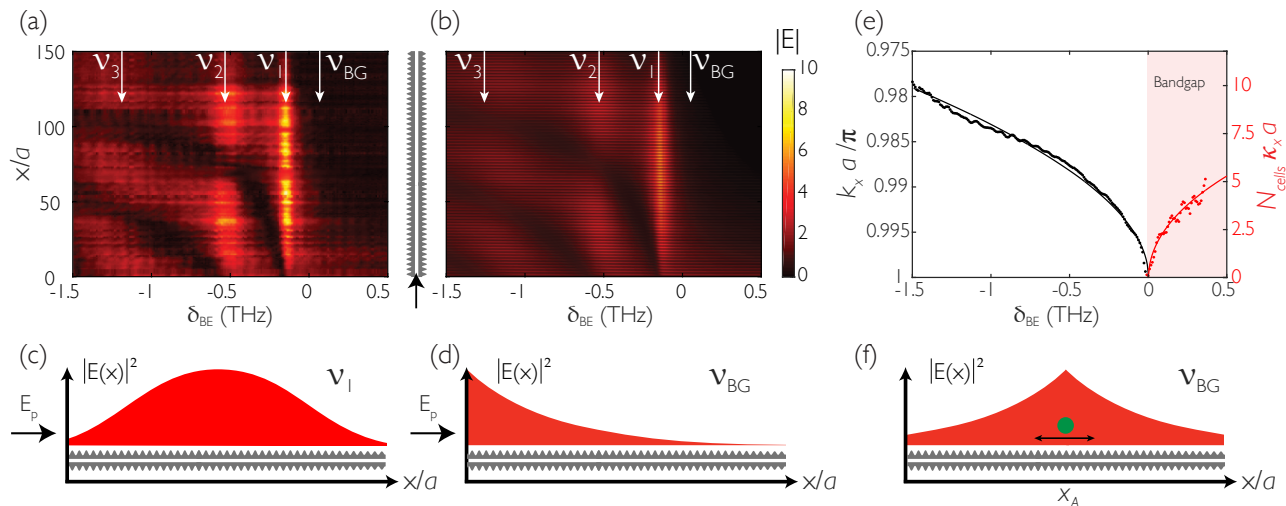


FIG. 2: Characterization of the alligator APCW. **(a)** Measured and **(b)** calculated electric field magnitude along the APCW, as functions of position x along the APCW and probe detuning $\delta_{\text{BE}} = \nu_p - \nu_{\text{BE}}$ relative to ν_{BE} for the dielectric band edge. **(c,d)** Guided mode intensity $|E(x)|^2$ at two different frequencies: (c) ν_1 for the first cavity resonance showing a resonant ‘super mode’ and (d) ν_{BG} inside the bandgap displaying exponential decay ($N_{\text{cells}}\kappa_x a = 2.0$ at ν_{BG}). **(e)** Dispersion relation for the projected wave vector k_x and attenuation constant κ_x versus probe detuning δ_{BE} deduced for the APCW obtained by fitting the data in (a) to a model of the device [33]. The shaded pink area represents frequencies inside the bandgap. **(f)** Plot of the exponentially localized emission $e^{-2\kappa_x|x-x_A|}$ from an atom (green sphere) at position x_A with transition frequency $\nu_{\text{D1}} = \nu_{\text{BG}}$ inside the bandgap.

Using a model for the field in a finite photonic crystal [33], we fit the measured intensity for each frequency in Fig. 2(a) and Fig. 2(b) and extract δk_x and κ_x , thereby obtaining the dispersion relations shown in Fig. 2(e). Importantly, we determine the band edge frequency for the actual device to be $\nu_{\text{BE}} - \nu_1 = 133 \pm 9$ GHz relative to the readily measured first resonance at ν_1 , which is in good agreement with the FDTD simulated result of 135 GHz.

Both ν_1, ν_{BG} are relevant to our measurements of transmission spectra with trapped atoms. The presence of a ‘cavity’ mode at ν_1 implies that the emission of an atom with transition frequency $\nu_{\text{D1}} = \nu_1$ will generate a field inside the APCW with a similar spatial profile to that of the cavity mode, as shown in Fig. 2(c). By contrast, atomic emission in the regime with $\nu_{\text{D1}} = \nu_{\text{BG}}$ within the bandgap will excite an exponentially localized mode centered around x_A , as illustrated in Fig. 2(f).

Experiment.— Cs atoms are trapped 240 nm above the geometric center of the APCW, as shown in Fig. 1(a), using a similar experimental setup to that reported in Ref. [18]. Atoms are cooled and trapped in a MOT around the APCW, and then loaded into a dipole trap formed by the reflection from the device of a frequency red-detuned side illumination (SI) beam. The SI beam has a waist of 50 μm , and the polarization is aligned along the x axis for maximum reflection from the APCW. The $1/e$ trap life time is ~ 30 ms. From the trap properties (including the Casimir-Polder potential from the APCW surfaces) and estimated atomic temperature, we infer atomic localization along the x, y, z coordinates to be $\delta x \simeq \pm 6$ μm , $\delta y \simeq \delta z \simeq \pm 30$ nm.

After the atoms are loaded into the trap, we send a weak 5 ms probe beam E_p with frequency ν_p in either the TE or TM guided mode through the APCW and record the transmitted intensity $|t(\nu_p) E_p(\nu_p)|^2$. The probe beam scans near the Cs $6S_{1/2}, F = 3 \rightarrow 6P_{1/2}, F' = 4$ transition. Each experimental cycle runs at a fixed detuning $\Delta_A = \nu_p - \nu_{\text{D1}}$ relative to the free-space atomic transition frequency ν_{D1} . The band edge of the APCW is tuned thermally by shining an external heating beam on the chip. Hence, the Cs D₁ line can be aligned to be either outside or inside the bandgap. The transmission for each data point is normalized by the transmission with no atoms ($|t_0 E_p|^2$), resulting in a measurement of $T/T_0 \equiv |t/t_0|^2$. The logarithm of the measured and simulated transmission spectrum with no atoms $T_0 = |t_0(\nu_p)|^2$ is shown in Fig. 3(a).

Examples of transmission spectra with atoms are shown in Figs. 3(b-d). Note that the spectra are shifted 12.5 MHz due to the AC Stark shift of the dipole trap. We estimate an average atom number of $\bar{N} = 3.0 \pm 0.5$ by measuring the superradiant atomic decay rate when the atom frequency ν_{D1} is tuned to the first resonance ν_1 , as described in [18, 33]. Notably, the atomic spectra at the first ‘cavity’ resonance ν_1 exhibit a characteristic Lorentzian line shape, and they become more and more asymmetric as the frequency moves into the bandgap.

Transmission model.— We have developed a model to extract quantitative values for collective decay rates and frequency shifts from these atomic transmission spectra [31]. While the formalism of waveguide [35] and cavity QED is well suited for describing atoms coupled to uni-

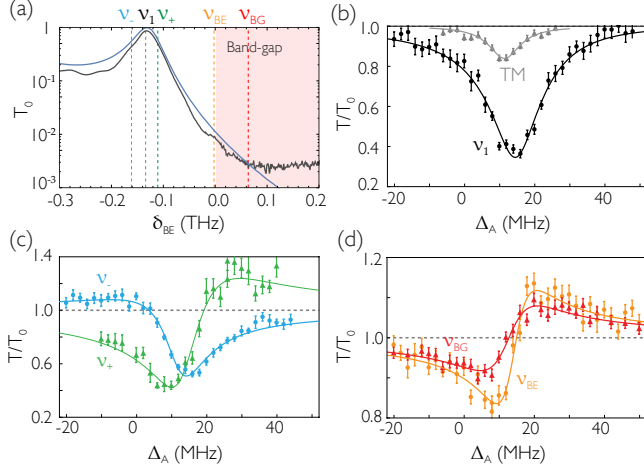


FIG. 3: Transmission spectra of the APCW with trapped atoms. **(a)** Measured (black) and FDTD simulated (blue) transmission spectra of the APCW without atoms as a function of the probe detuning from the band edge frequency, $\delta_{\text{BE}} = \nu_{\text{p}} - \nu_{\text{BE}}$. There is a minimum extinction of -25 dB for the transmitted signal due to fabrication imperfections. **(b-d)** Transmission spectrum for $\bar{N} = 3.0 \pm 0.5$ trapped atoms versus probe detuning $\Delta_{\text{A}} = \nu_{\text{p}} - \nu_{\text{D1}}$, at several frequencies around the band edge. The solid lines are fits using the transmission model in Eq. (4), averaged over atom positions and different atom numbers. In **(b)**, the Cs D₁ line is aligned to the first ‘cavity’ resonance ν_1 , resulting in symmetric spectra for both the TE (black) and TM (gray) modes. The TE spectra in **(c)** are for frequencies $\nu_{-/+}$ on the two sides of the resonance. The TE spectra in **(d)** are taken at the band edge (ν_{BE} , circles) and 60 GHz (ν_{BG} , triangles) into the bandgap. The asymmetry of the line-shapes implies a large ratio of coherent to dissipative interactions.

form waveguides and cavities, it is not general enough to capture the rich physics of atomic interactions in the vicinity of an APCW. Instead, we describe our system by employing a spin model in terms of the classical electromagnetic Green’s function, in which the atoms (or ‘spins’) interact via the emission and re-absorption of guided photons [36–38]. While the atomic degrees of freedom themselves may be quantum mechanical, the spatial character of photons propagating between them can be understood classically and is encoded in the electromagnetic Green’s function.

Within the Markov approximation, the master equation for the atomic density matrix in the frame rotating at the probe laser frequency is $\dot{\hat{\rho}}_{\text{A}} = -\frac{i}{\hbar}[\mathcal{H}, \hat{\rho}_{\text{A}}] + \mathcal{L}[\hat{\rho}_{\text{A}}]$, where the Hamiltonian and Lindblad operators read

$$H = -\hbar \sum_{j=1}^N \left[\tilde{\Delta}_{\text{A}} \hat{\sigma}_{ee}^j + (\Omega_j \hat{\sigma}_{eg}^j + \Omega_j^* \hat{\sigma}_{ge}^j) + \sum_{i=1}^N J_{\text{1D}}^{ji} \hat{\sigma}_{eg}^j \hat{\sigma}_{ge}^i \right], \quad (1a)$$

$$\mathcal{L}[\rho_{\text{A}}] = \sum_{j,i=1}^N \frac{\Gamma' \delta_{ji} + \Gamma_{\text{1D}}^{ji}}{2} \times (2\hat{\sigma}_{ge}^j \hat{\rho}_{\text{A}} \hat{\sigma}_{eg}^i - \hat{\sigma}_{eg}^j \hat{\sigma}_{ge}^i \hat{\rho}_{\text{A}} - \hat{\rho}_{\text{A}} \hat{\sigma}_{eg}^j \hat{\sigma}_{ge}^i), \quad (1b)$$

where N is the number of atoms, $\tilde{\Delta}_{\text{A}} = 2\pi\Delta_{\text{A}} = 2\pi(\nu_{\text{p}} - \nu_{\text{D1}})$ is the detuning between the probe and the atomic angular frequencies, Ω_j is the Rabi frequency for atom j due to the guided mode field, $\hat{\sigma}_{ge}^j = |g\rangle\langle e|$ is the atomic coherence operator between the ground and excited states of atom j , and δ_{ji} is the Kronecker delta.

The coherent evolution of the atoms is determined by the Hamiltonian, whose terms represent the free atomic evolution, the GM probe drive, and the spin-exchange, respectively. The Lindblad term is responsible for the dissipative interactions, which include atomic decay into non-guided (Γ') and guided (Γ_{1D}^{ji}) modes. For low atomic density along the APCW, the non-guided emission is not cooperative, and is described here as a single-atom effect.

The atom-atom spin-exchange rate is expressed in terms of the real part of the guided mode Green’s function as $J_{\text{1D}}^{ji} = \mu_0 \omega_{\text{p}}^2 \mathbf{d}_j^* \cdot \text{Re} \mathbf{G}(\mathbf{r}_j, \mathbf{r}_i, \omega_{\text{p}}) \cdot \mathbf{d}_i$, and the decay rate into the guided mode is written in terms of the imaginary part as $\Gamma_{\text{1D}}^{ji} = 2\mu_0 \omega_{\text{p}}^2 \mathbf{d}_j^* \cdot \text{Im} \mathbf{G}(\mathbf{r}_j, \mathbf{r}_i, \omega_{\text{p}}) \cdot \mathbf{d}_i$, where $\omega_{\text{p}} = 2\pi\nu_{\text{p}}$ and \mathbf{d}_j is the dipole moment of atom j . The appearance of the real and imaginary parts of the Green’s function in the coherent and dissipative terms has the classical analogue that the in-phase and out-of-phase components of a field with respect to an oscillating dipole store time-averaged energy and perform time-averaged work, respectively.

In the low saturation regime, the Heisenberg equation for the expectation value of the atomic coherences ($\langle \hat{\sigma}_{eg} \rangle = \sigma_{eg}$) is simply

$$\dot{\sigma}_{ge}^j = i \left(\tilde{\Delta}_{\text{A}} + i \frac{\Gamma'}{2} \right) \sigma_{ge}^j + i \Omega_j + i \sum_{i=1}^N h^{ji} \sigma_{ge}^i, \quad (2)$$

where $h^{ji} = J_{\text{1D}}^{ji} + i\Gamma_{\text{1D}}^{ji}/2$ derives from the projection of the Green’s function onto the dipoles $\mathbf{d}_{j,i}$ of atoms j, i . The atomic coherences σ_{ge}^j are solved for by diagonalizing the matrix \mathcal{H} , whose elements are h^{ji} . The dynamics of the atoms can then be understood in terms of the eigenvalues and eigenfunctions of \mathcal{H} , where the real and imaginary parts of the eigenvalues correspond to frequency shifts and decay rates due to the guided mode.

For non-interacting atoms, \mathcal{H} is diagonal, the eigenvalues are $h^{ii} = J_{\text{1D}}^{ii} + i\Gamma_{\text{1D}}^{ii}/2$ for $i = \{1, N\}$, and there is no cooperative response.

In contrast, for interacting atoms, the off-diagonal components of \mathcal{H} are non-negligible. In particular, for the atomic frequency inside the bandgap of a photonic crystal, the elements of \mathcal{H} are well approximated by

$$h^{ji} = h \cos(\pi x_j/a) \cos(\pi x_i/a) e^{-\kappa_x |x_j - x_i|}, \quad (3)$$

where the cosine factors arise from the Bloch mode and κ_x^{-1} gives the finite range of interaction, due to the localization of the field.

For the case when the interaction range is much larger than the spacing of the atoms ($\delta x \kappa_x \ll 1$), the diagonal h^{ii} and off-diagonal h^{ji} elements of \mathcal{H} are generally of comparable magnitude, with the off-diagonal elements expressing coherences between atoms. Furthermore, h^{ji} is separable, which results in eigenvalues $(\lambda_B, 0, \dots, 0)$, where $\lambda_B = \sum_{i=1}^N h^{ii} = \sum_{i=1}^N (J_{1D}^{ii} + i\Gamma_{1D}^{ii}/2) \equiv J_{1D}^{(N)} + i\Gamma_{1D}^{(N)}/2$. The eigenvalue λ_B represents an atomic ‘bright mode’ spawned by the GM probe field. The atoms behave as a single ‘super-atom’ whose frequency shift and decay rate derive from atom-atom coherences expressed by off-diagonal elements h^{ji} . In the current limit of $\delta x \kappa_x \ll 1$, this situation is analogous to cQED where atoms couple to a single mode of a high finesse optical resonator [23].

Given the steady-state solution for the atomic coherences σ_{ge}^j from the diagonalization of \mathcal{H} , we determine the field along the APCW by means of a generalized input-output equation that involves the Green’s function of the structure and σ_{ge}^j [31]. Physically, the total field is the sum of the input probe and the fields re-scattered by the atoms.

The normalized transmission then reads [31]

$$\frac{t(\tilde{\Delta}_A, N)}{t_0(\tilde{\Delta}_A)} = \frac{\tilde{\Delta}_A + i\Gamma'/2}{\left(\tilde{\Delta}_A + J_{1D}^{(N)}\right) + i\left(\Gamma' + \Gamma_{1D}^{(N)}\right)/2}, \quad (4)$$

where, as before, $t_0(\tilde{\Delta}_A)$ is the transmission of the APCW without the atoms. We obtain this equation by assuming that the GM has linear polarization, as it is mainly y -polarized in the central plane of the APCW.

The single ‘bright mode’ picture is valid over the range of frequencies of our measured spectra in Fig. 3. In particular, at the furthest frequency into the bandgap $\Delta_{BE} = 60$ GHz, we have that $\delta x \kappa_x \simeq 0.2$. However, for atomic frequencies further away from the band edge, this approximation eventually breaks down (e.g., at the bandgap center, $\delta x \kappa_x \simeq 1.5$).

Measurements and analysis.— Equation (4) provides a direct mapping between the observed atomic spectra of Figs. 3(b-d) and the electromagnetic Green’s function of the APCW. In particular, the line shape is Lorentzian for purely dissipative dynamics ($J_{1D}^{(N)} = 0$). This is precisely what occurs at the frequency of the first cavity mode ν_1 , as shown by Fig. 3(b). When the GM probe frequency moves towards the band edge, the dispersive interactions are switched on, and the line shape becomes asymmetric, displaying a Fano resonance [39], as can be observed in Figs. 3(c,d). Therefore, the appearance of an asymmetry in the atomic spectra directly unveils significant coherent behavior between the atoms, which is evident for frequencies that lie in the bandgap region. For all relevant frequencies, the TM spectrum is always symmetric,

as $J_{1D}^{\text{TM}}, \Gamma_{1D}^{\text{TM}} \ll \Gamma'$ for this GM polarization.

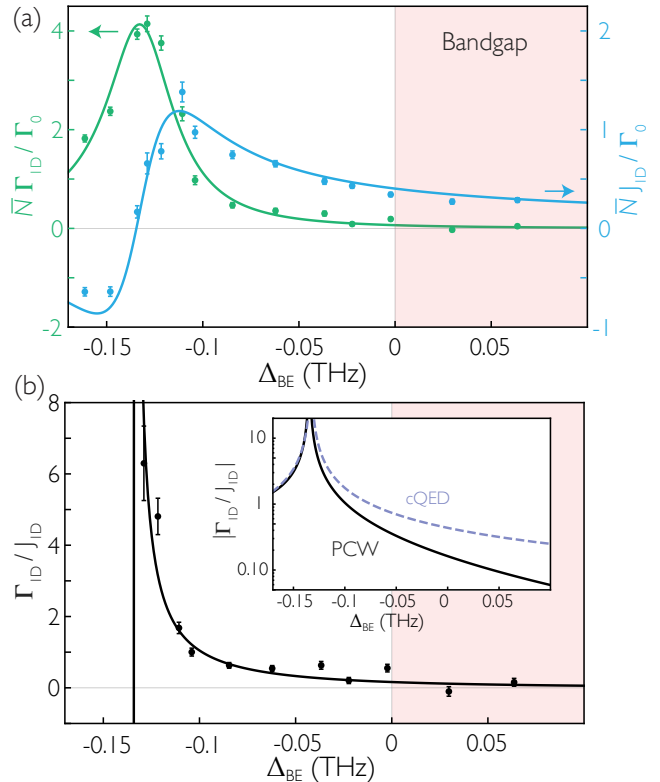


FIG. 4: **(a)** Peak coherent interaction rate $\bar{N}\Gamma_{1D}$ (green) and dissipation rate $\bar{N}J_{1D}$ (blue) around the band edge. With \bar{N} determined from independent decay rate measurements, the values for Γ_{1D}, J_{1D} are found from fits of the transmission model in Eq. (4) to the measured atomic spectra and are normalized by the free-space decay rate $\Gamma_0 = 2\pi \times 4.56$ MHz for the Cs D₁ line. The probe couples to a collective mode and therefore is sensitive to the product of \bar{N} and the rates. The lines are the predictions from a numerical model based on 1D transfer matrices [40]. **(b)** The measured and calculated ratios $\mathcal{R} = \Gamma_{1D}/J_{1D}$. The average of the two points in the bandgap gives that the ratio of the dissipative to coherent coupling rate is $\mathcal{R} = 0.05 \pm 0.17$. The inset is a comparison of \mathcal{R} for the APCW calculation (solid) and cQED model (dashed). From the measured linewidth of the first cavity resonance, $\gamma_c = 60 \pm 8$ GHz, cQED predicts that $\mathcal{R}_{\text{cQED}} = \gamma_c/\Delta_c$, where $\Delta_c = (\nu_p - \nu_1)$.

Furthermore, we can obtain quantitative values for the collective frequency shifts and decay rates by fitting the atomic spectra to the spin model, once we account for the uncertainties in atom number and positions. As described in Ref. [18] and depicted in Fig. 1(a), trapped atoms are free to move along the x -axis. Their coupling rates are thus modulated by the fast oscillation of the Bloch function, which near the band edge is approximately given by $\Gamma_{1D}^{ii}(x_i) = \Gamma_{1D} \cos^2(x_i\pi/a)$ and $J_{1D}^{ii}(x_i) = J_{1D} \cos^2(x_i\pi/a)$. Here Γ_{1D} and J_{1D} are the peak values. Further, although we know the average atom number is $\bar{N} \sim 3$ from decay rate measurements

[33], the atom number for each experiment is random. To model the experimental transmission spectra, we average the expression in Eq. (4) over the atom positions $\{x_i\}$ along the Bloch function and assume a Poisson distribution in atom number with mean \bar{N} . We extract peak values Γ_{1D} and J_{1D} for the independently determined \bar{N} , and plot the resulting cooperative rates $\bar{N}\Gamma_{1D}$ and $\bar{N}J_{1D}$ in Fig. 4(a). We also fit for the non-guided radiative decay Γ' and a frequency shift Δ_0 to account for the AC Stark shift induced by the dipole trap light, as described in the supplemental material [33]. Due to inhomogeneous broadening, we measure $\Gamma' = 2\pi \times 9.1$ MHz, which is larger than the simulated value of $\Gamma' = 2\pi \times 5.0$ MHz [33].

The ratio $\mathcal{R} = \Gamma_{1D}/J_{1D}$ is shown in Fig. 4(b). Because of the evanescent nature of the field in the bandgap, \mathcal{R} decays exponentially with increasing detuning into the bandgap, $\mathcal{R} \sim e^{-\kappa_x L}$, where $\kappa_x \propto \sqrt{\Delta_{BE}}$ [23]. As displayed in the inset, the ratio between the frequency shift and the GM decay rate diminishes much faster than would be the case in traditional settings such as cQED, for which $\mathcal{R}_{cQED} = \gamma_c/\Delta_c$, where γ_c is the cavity linewidth and Δ_c is the detuning from the cavity resonance. Indeed, by performing an average of the last two measured frequencies in the bandgap, we obtain $\mathcal{R} = 0.05 \pm 0.17$, whereas $\mathcal{R}_{cQED} = 0.30 \pm 0.04$, where we have taken the cavity linewidth to be a value consistent with the linewidth of the first cavity mode of the APCW ($\gamma_c = 60 \pm 8$ GHz). We can then infer that the ratio of dispersive to dissipative rates for guided mode atom-atom interactions (i.e., $1/\mathcal{R}$) is significantly larger than is the case in conventional optical physics (e.g., cQED).

Despite favorable scaling between the collective frequency shifts and the guided mode decay rates, there is still one obstacle to overcome towards purely dispersive atomic interactions, namely atomic emission into non-guided modes (characterized by Γ'). For the current APCW structure, the FDTD simulated value of this decay rate is $\Gamma' \simeq 1.1\Gamma_0$ [18] for the relevant frequencies of our experiment. Fortunately, it has been shown that suitable engineering of a wide variety of nanophotonic structures can lead to significant reductions in Γ'/Γ_0 . For example, Ref. [1] reviews possibilities to achieve $\Gamma' \simeq 0.1\Gamma_0$.

Concluding remarks and outlook.— In conclusion, we report the first observation of cooperative atom interactions in the bandgap of a photonic crystal waveguide. By tuning the band edge frequency of the photonic crystal waveguide, we are able to modify the interactions between the atoms that are trapped close to the device, reducing the dissipative relative to coherent coupling for frequencies inside the bandgap of the PCW. Equipped with a theoretical model based on the electromagnetic Green's function of the alligator photonic crystal waveguide, we infer quantitative values for the collective frequency shifts and decay rates experienced by the atoms. Moreover, we infer a suppression of the dissipative inter-

actions with respect to the coherent ones several times larger than is customarily obtained in cQED. Our measurements provide the first stepping stone towards the realization of quantum many body physics in bandgap systems.

This work opens the door to exploring new physical scenarios employing atoms coupled to PCWs. By trapping the atoms at the center of the device with guided modes, we expect a 6-fold increase to both coupling strengths J_{1D} and Γ_{1D} relative to Γ' . Moreover, by probing the atoms with Cs tuned to the upper band edge, where the intensity at the position of the atoms is larger, we expect a further improvement by a factor of two. Combining these two effects, we expect a significant enhancement of interactions via the preferred modes over free space. This will allow us to study new paradigms for atom-photon interactions, such as the recently proposed multi-photon dressed states [41, 42].

Acknowledgments.— We gratefully acknowledge the contributions of O. J. Painter and his group, including for fabrication and clean-room facilities. We further acknowledge A. Burgers, C.-L. Hung, J. Laurat, M. J. Martin, A. C. McClung, J. A. Muniz, and L. Peng. Funding is provided by the DOD NSSEFF program, the AFOSR QuMPASS MURI, NSF Grant PHY-1205729 the ONR QOMAND MURI, and the IQIM, an NSF Physics Frontiers Center with support of the Moore Foundation. A. G. was supported by the Nakajima Foundation. A. A.-G. and M. L. were supported by the IQIM Postdoctoral Fellowship. A. A.-G. also acknowledges support from the Global Marie Curie Fellowship LANTERN (655701). S.-P. Y. acknowledges support from the International Fulbright Science and Technology Award. DEC acknowledges support from Fundacio Privada Cellex Barcelona, Marie Curie CIG ATOMNANO, MINECO Severo Ochoa Grant SEV-2015-0522, and ERC Starting Grant FoQAL.

-
- [1] Lodahl P, Mahmoodian S, Stobbe S (2015) Interfacing single photons and single quantum dots with photonic nanostructures. *Nature* 520:452–458.
 - [2] Kimble HJ (2008) The quantum internet. *Nature* 453:1023–1030.
 - [3] Vuckovic J, Yamamoto Y (2003) Photonic crystal microcavities for cavity quantum electrodynamics with a single quantum dot. *App. Phys. Lett.* 82:2374–2376.
 - [4] Yoshie T et al. (2004) Vacuum Rabi splitting with a single quantum dot in a photonic crystal nanocavity. *Nature* 432:200–203.
 - [5] Aoki T et al. (2006) Observation of strong coupling between one atom and a monolithic microresonator. *Nature* 443:671.
 - [6] Hennessy K et al. (2007) Quantum nature of a strongly coupled single quantum dot-cavity system. *Nature* 445:896–899.
 - [7] Thompson JD et al. (2013) Coupling a single trapped

- atom to a nanoscale optical cavity. *Science* 6137:1202–1205.
- [8] Bajcsy M et al. (2009) Efficient all-optical switching using slow light within a hollow fiber. *Phys. Rev. Lett.* 102:203902.
- [9] Balykin VI, Hakuta K, Kien FL, Liang JQ, Morinaga M (2004) Atom trapping and guiding with a subwavelength-diameter optical fiber. *Phys. Rev. A* 70:011401.
- [10] Londero P, Venkataraman V, Bhagwat AR, Slepko AD, Gaeta AL (2009) Ultralow-power four-wave mixing with rb in a hollow-core photonic band-gap fiber. *Phys. Rev. Lett.* 103:043602.
- [11] Vetsch E et al. (2010) Optical interface created by laser-cooled atoms trapped in the evanescent field surrounding an optical nanofiber. *Phys. Rev. Lett.* 104:203603.
- [12] Goban A et al. (2012) Demonstration of a state-insensitive, compensated nanofiber trap. *Phys. Rev. Lett.* 109:033603.
- [13] Sørensen HL et al. (2016), arXiv:1601.04869.
- [14] Chang DE, Sørensen AS, Demler EA, Lukin MD (2007) A single-photon transistor using nanoscale surface plasmons. *Nat. Phys.* 3:807–812.
- [15] Akimov AV et al. (2007) Generation of single optical plasmons in metallic nanowires coupled to quantum dots. *Nature* 450:402–406.
- [16] Huck A, Kumar S, Shakoor A, Andersen UL (2011) Controlled coupling of a single nitrogen-vacancy center to a silver nanowire. *Phys. Rev. Lett.* 106:096801.
- [17] Joannopoulos JD, Meade RD, Winn JN (1995) *Photonic Crystals: Molding the Flow of Light*. (Princeton University Press, Singapore).
- [18] Goban A et al. (2015) Superradiance for atoms trapped along a photonic crystal waveguide. *Phys. Rev. Lett.* 115:063601.
- [19] Yablonovitch E (1987) Inhibited spontaneous emission in solid-state physics and electronics. *Phys. Rev. Lett.* 58:2059.
- [20] John S (1987) Strong localization of photons in certain disordered dielectric superlattices. *Phys. Rev. Lett.* 58:2486.
- [21] John S, Wang J (1990) Quantum electrodynamics near a photonic band gap: photon bound states and dressed atoms. *Phys. Rev. Lett.* 64:2418.
- [22] Kurizki G (1990) Two-atom resonant radiative coupling in photonic band structures. *Phys. Rev. A* 42:2915.
- [23] Douglas JS et al. (2015) Quantum many-body models with cold atoms coupled to photonic crystals. *Nat. Photon.* 9:326–331.
- [24] González-Tudela A, Hung CL, Chang DE, Cirac JI, Kimble HJ (2015) Subwavelength vacuum lattices and atom-atom interactions in two-dimensional photonic crystals. *Nat. Photon.* 9:320–325.
- [25] Hartmann MJ, Brandão FGSL, Plenio MB (2006) Strongly interacting polaritons in coupled arrays of cavities. *Nat. Phys.* 2:849–855.
- [26] Greentree AD, Tahan C, Cole JH, Hollenberg LCL (2006) Quantum phase transitions of light. *Nat. Comm.* 2:856–861.
- [27] Goban A et al. (2014) Atom-light interactions in photonic crystals. *Nat. Comm.* 5:3808.
- [28] Yu SP et al. (2014) Nanowire photonic crystal waveguides for single-atom trapping and strong light-matter interactions. *App. Phys. Lett.* 104:111103.
- [29] Lund-Hansen T et al. (2008) Experimental realization of highly efficient broadband coupling of single quantum dots to a photonics crystal waveguide. *Phys. Rev. Lett.* 101:113903.
- [30] Young AB et al. (2015) Polarization engineering in photonic crystal waveguides for spin-photon entanglers. *Phys. Rev. Lett.* 115:153901.
- [31] Asenjo-Garcia A, Hood JD, Chang DE, Kimble HJ (2016), in preparation.
- [32] COMSOL, <http://www.comsol.com>.
- [33] See accompanying Supplemental Material for a thorough description of the design and characterization of the photonic crystal waveguide; of how to obtain the attenuation coefficient and the band-edge position of the PCW; of how to generate the atomic spectra fits; and of the measurements of atomic decay.
- [34] Lumerical Solutions, Inc., <http://www.lumerical.com/tcad-products/fdtd/>.
- [35] Sheng JT, Fan S (2005) Coherent photon transport from spontaneous emission in one-dimensional waveguides. *Opt. Lett.* 30:2001.
- [36] Dung HT, Knöll L, Welsch DG (2002) Resonant dipole-dipole interaction in the presence of dispersing and absorbing surroundings. *Phys. Rev. A* 66:063810.
- [37] Buhmann SY, Welsch DG (2007) Dispersion forces in macroscopic quantum electrodynamics. *Prog. Quantum Electron.* 31:51.
- [38] Dzsotjan D, Sørensen A, Fleischhauer M (2010) Quantum emitters coupled to surface plasmons of a nanowire: A Green's function approach. *Phys. Rev. B* 82(7):075427.
- [39] Fano U (1961) Effects of configuration interaction on intensities and phase shifts. *Phys. Rev.* 124:1866–1878.
- [40] Hood JD et al., in preparation (2016).
- [41] Calajó G, Ciccarello F, Chang DE, Rabl P (2015), arXiv:1512.04946.
- [42] Shi T, Wu YH, González-Tudela A, Cirac JI (2015), arXiv:1512.072338.

Supplemental Information: Atom-atom interactions around the band edge of a photonic crystal waveguide

ALLIGATOR PHOTONIC CRYSTAL WAVEGUIDE DESIGN AND FABRICATION

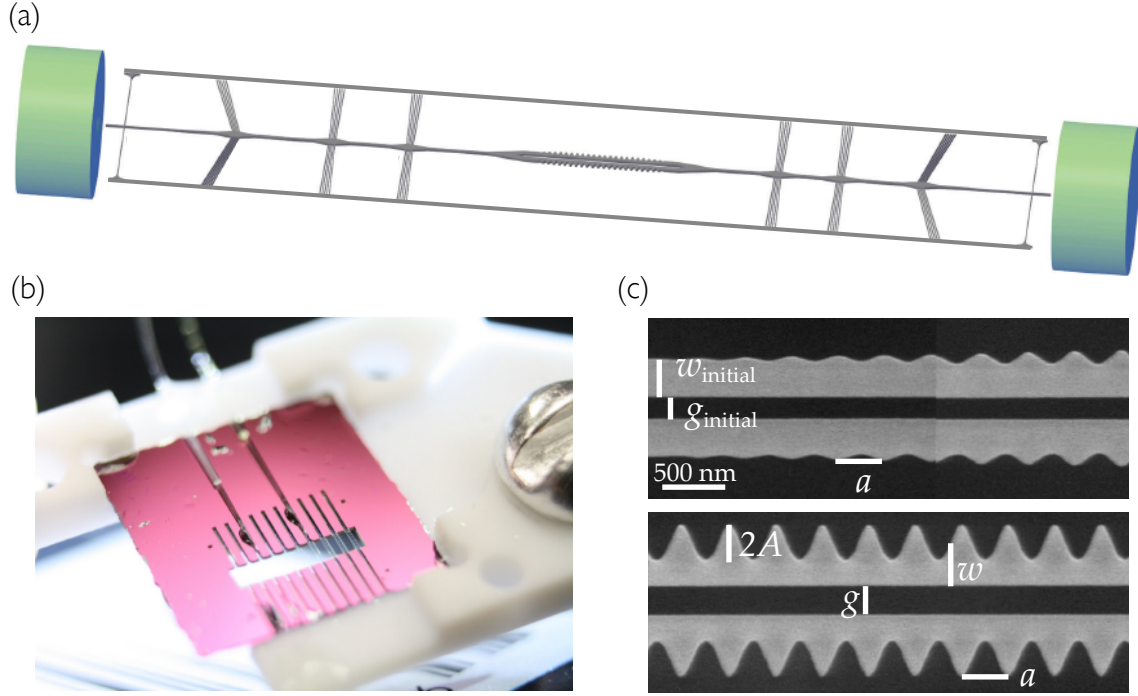


FIG. S1: Alligator photonic crystal waveguide (APCW) chip and device overview, taken from Ref. [S1]. **(a)** Schematic of the entire device. The alligator photonic crystal waveguide (APCW) is at the center. Optical fibers (green) on both sides couple light into and out of the waveguide. The waveguide is surrounded by supporting and cooling structures. **(b)** Image of a 10×10 mm APCW chip, taken from Ref. [S1]. Multiple waveguides stretch across the window of the chip, with the APCWs at the center of the window. The window provides optical access for trapping and cooling atoms around the device. **(c)** Overview of device variables. The lattice constant for the entire device is $a = 370$ nm. The device dimensions are measured with an SEM and are calibrated to the lattice constant. The device dimensions are $w = 310 \pm 10$ nm, $2A = 262 \pm 10$ nm, $g = 220 \pm 10$ nm, $w_{\text{initial}} = 268 \pm 15$ nm, $g_{\text{initial}} = 165 \pm 10$ nm. The thickness of the silicon nitride is 185 ± 5 nm. The index of refraction for Si_3N_4 is $n = 2.0$ around our frequencies of interest.

The schematic of the device is shown in Fig. S1(a). Light is coupled into and out of the device by mode-matching the output of an optical fiber to that of a terminated rectangular-shaped waveguide on both sides of the device [S1]. The fibers are glued permanently in etched v-grooves at optimized coupling positions. The design and fabrication of the alligator photonic crystal waveguide (APCW) are detailed in Ref. [S1]. The APCW is fabricated on a $200 \mu\text{m}$ silicon (Si) chip coated with a 200 nm thick silicon nitride (SiN) film. The SiN device is suspended across a 2 -mm-wide window after the silicon substrate beneath it is removed, as shown in the image of Fig. S1(b). The window allows optical access for the trapping and cooling of atoms around the device.

The dielectric TE mode band edge (ν_{BE}) is aligned to within 200 GHz of the Cs D1 line ($\nu_{\text{D1}} = 335.12$ THz) via a low-power inductively-coupled reactive-ion CF_4 etch. The directional etch thins the SiN layer at a rate of 3 nm/min until a transmission measurement confirms alignment of the band edge. The final geometric dimensions of the device used in the main text are given in Fig. S1(c).

For the experiment, the chip is placed at the center of a ultra-high vacuum chamber, and the optical fibers exit through Teflon fiber feed-throughs. We measure the transmission through a device using a super luminescent diode (SLD) as the source and an optical spectrum analyzer (OSA) as the detector. The measured transmission and

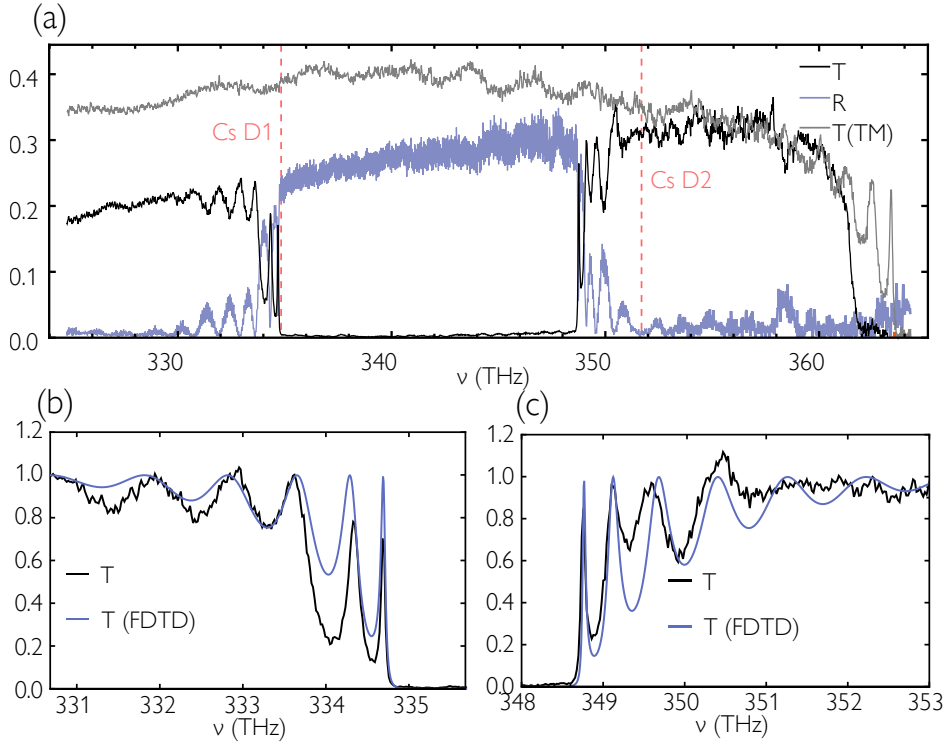


FIG. S2: Measured and simulated transmission and reflection spectra. **(a)** Transmission (black) and reflection (blue) spectra through the entire chip for the TE mode (polarization in the plane of the device). The red dashed lines are the Cs D₁ (335.1 THz) and D₂ (351.7 THz) lines. The TE transmission efficiency through the entire device near the dielectric band edge is $\sim 23\%$, indicating that the single pass efficiency from the fiber to device is approximately 49%. Most of the loss is due to the waveguide-to-fiber coupling section. The gray line is the TM transmission (polarization out of the plane of the device). Note that the lower band edge of the TM mode is visible at around 365 THz, but is far detuned from both Cs D₁ transitions. **(b-c)** TE transmission data is normalized and compared to a finite-difference time-domain (FDTD) simulation. A commercial simulator based on the FDTD method was used to perform the calculations [S2]. The simulation uses the measured device parameters in Fig. S1, but adjusted within the uncertainty of the measurements so that the position of the first resonances match those in the measured spectra.

reflection spectra are shown in Fig. S2(a). The transmission spectra near the lower (dielectric) and upper (air) band edge are compared to an FDTD simulation in Fig. S2(b-c).

ALLIGATOR DISPERSION RELATION FROM SCATTERING IMAGES

Here, we describe the analysis performed for the APCW dispersion relations in Fig. 2(e) of the manuscript. We send a single-frequency laser beam through the device and image the scattered light with a microscope. We integrate the image over the width of the APCW to produce a single plot of intensity versus position. Then we scan the laser frequency around the lower band edge to produce a 2D plot of scattered intensity as a function of position and frequency.

The weak scattered light comes from small fabrication imperfections or intrinsic material defects and serves as a probe of the local intensity. Since each scatterer emits light at a different rate, we have to normalize the scattered light by a reference intensity spectrum in which the intensity of the device is known. For this reference spectrum, we average over the intensities for frequencies far from the band edge, where the APCW behaves like a waveguide, and where the local intensity in the device is approximately constant. The normalized data is shown in Fig. S3, and a zoomed-in version is in Fig. 2(a) of the manuscript.

In the FDTD simulation described above, we measure the intensity along the center of the device for frequencies around the band edge. Taking the maximum intensity in each unit cell and normalizing by the intensity in the waveguide regime, we produce Fig. 2(b) in the main text.

Next, we fit the intensity spectrum at a given frequency to a model in order to extract the wave-vector for that

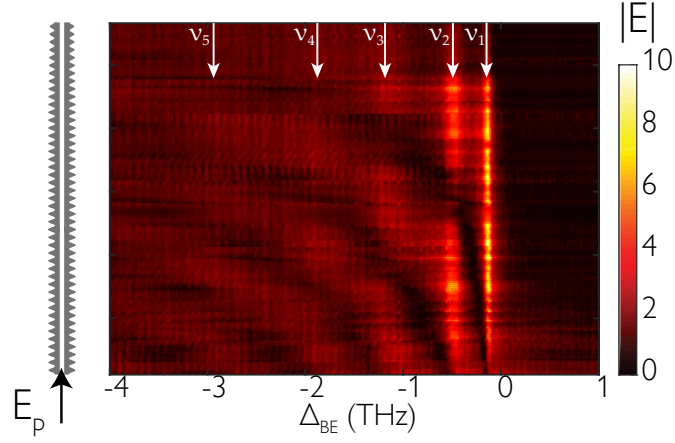


FIG. S3: Normalized magnitude of the scattered electric field of the APCW for frequencies $\Delta_{\text{BE}} = \nu_p - \nu_{\text{BE}}$ around the band edge.

frequency. Near the band edge, the field in an infinite APCW is well approximated by $E(x) \propto \cos(x\pi/a)e^{i\delta k_x x}$, where $\delta k_x = \pi/a - k_x$ in the propagating band ($\Delta_{\text{BE}} < 0$) and $\delta k_x = i\kappa_x$ inside the bandgap ($\Delta_{\text{BE}} > 0$) [S3]. The edges of a finite photonic crystal reflect with R_t due to a large group index mismatch between the waveguide section and the photonic crystal waveguide. The resonances of the weak cavity result in the cavity-like intensity profiles seen at frequencies $\nu_{1,2,3,4,5}$ in Fig. S3. The intensity at a point x along a finite photonic crystal of length L is well approximated by a model based on the intensity in a cavity with two mirrors of reflectivity R_t [S3],

$$|E(x)|^2 = I_1 |e^{i\delta k_x x} - R_t e^{2i\delta k_x L} e^{-i\delta k_x x}|^2, \quad (\text{S1})$$

where I_1 is related to the overall intensity. This expression ignores the fast oscillations of the Bloch function, which goes as $\cos^2(x\pi/a)$. Note that in the bandgap (when $\kappa_x L \gg 1$), the intensity model reduces to an exponential decay: $|E(x)|^2 \approx I_1 e^{-2\kappa_x x}$. Interestingly, at the band edge ($\delta k_x \rightarrow 0$, $R_t \rightarrow 1$), the intensity displays a quadratic dependence on the position, $|E(x)|^2 \propto (L - x)^2$.

For each frequency, we fit the intensity along the nominal cells with Eq. (S1) and extract δk_x . This procedure allows us to map out the dispersion relation $\delta k_x(\Delta_{\text{BE}})$, which we show in Fig. 2(e) for the measured and simulated data. From the simulated fits, we find that the effective length of the cavity is 162 cells, which is slightly longer than the 150 nominal cells. This is expected since the cavity field can leak into the tapering sections. We use this length for the fits of the measured data. Examples of the measured and simulated intensity are shown in Fig. S4.

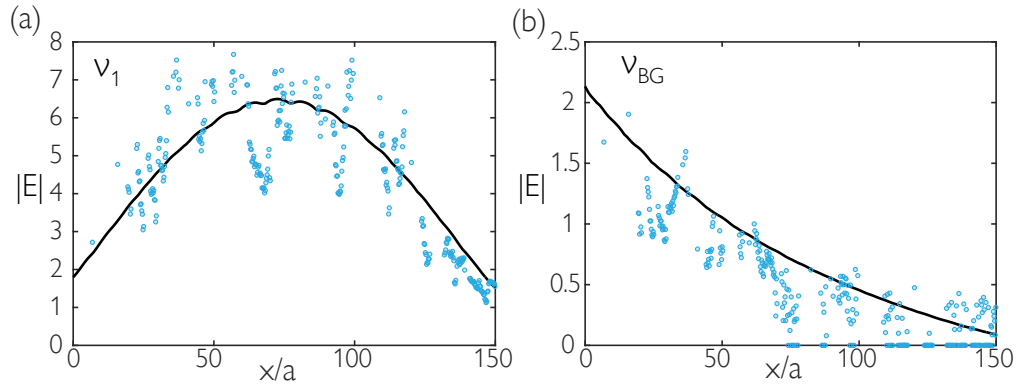


FIG. S4: The electric field magnitude in the APCW at the first resonance ν_1 (a), and in the bandgap $\nu_{\text{BG}} = \nu_{\text{BE}} + 60$ GHz (b). The points show measured data, and the black lines are from an FDTD simulation. The electric field magnitude $|E|$ is normalized by the electric field magnitude far from the band edge; thus, these plots gives the enhancement of $|E|$ over the waveguide regime.

The frequency for which $\delta k_x = 0$ is defined as the band edge frequency ν_{BE} . To extract this frequency and the curvature of the dispersion relation near the band edge, we fit the measured and simulated dispersion relations with

a dispersion model [S3, S4],

$$\delta k_x(\nu) = \frac{2\pi}{a} \sqrt{\frac{(\nu_{\text{BE}2} - \nu)(\nu_{\text{BE}} - \nu)}{4\zeta^2 - (\nu_{\text{BE}2} - \nu_{\text{BE}})^2}}, \quad (\text{S2})$$

where ν_{BE} ($\nu_{\text{BE}2}$) is the lower (upper) band edge frequency, and ζ is a frequency related to the curvature of the band near the band edge. From the measured data fits, the distance between the first resonance and band edge is $\nu_{\text{BE}} - \nu_1 = 133 \pm 9$ GHz and $\zeta = 227 \pm 3$ THz. The simulated data gives $\nu_{\text{BE}} - \nu_1 = 135.0$ GHz and the curvature parameter is $\zeta = 226.0$ THz. These values are in good agreement with the dispersion relation from the eigenmode simulation of the infinite APCW in Fig. 1(c) of the main text, which gives $\zeta = 229.1$ THz.

ATOMIC SPECTRA FITS

Here, we discuss the transmission model used to extract the dissipative and dispersive interaction rates from the atomic transmission spectra. As discussed in the main text, the transmission expression is derived by substituting the solution of the steady state atomic coherences σ_{ge} into a generalized input-output equation that relates the electric field along the APCW to the scattering from the atoms [S5],

$$\hat{\mathbf{E}}^+(\mathbf{r}, \omega_p) = \hat{\mathbf{E}}_p^+(\mathbf{r}, \omega_p) + \mu_0 \omega_p^2 \sum_j \mathbf{G}(\mathbf{r}, \mathbf{r}_j, \omega_p) \cdot \mathbf{d}_j \hat{\sigma}_{ge}^j. \quad (\text{S3})$$

Here, $\hat{\mathbf{E}}^+$ and $\hat{\mathbf{E}}_p^+$ are the positive-frequency components of the total and probe electric field operators, respectively.

For frequencies near the band-edge of a PCW and when the interaction range is much larger than the atomic spacing, the dispersive and dissipative couplings between atoms j and i are well approximated by

$$J_{1D}^{ji} = J_{1D} \cos(x_j \pi/a) \cos(x_i \pi/a) \quad \text{and} \quad \Gamma_{1D}^{ji} = \Gamma_{1D} \cos(x_j \pi/a) \cos(x_i \pi/a). \quad (\text{S4})$$

In this system, there is only a single atomic ‘bright mode’, for which the frequency shift and guided-mode decay rate are given by $J_{1D}^{(N)} = \sum_{i=1}^N J_{1D}^{ii}$ and $\Gamma_{1D}^{(N)} = \sum_{i=1}^N \Gamma_{1D}^{ii}$. In this single bright mode approximation, the transmission spectra for N atoms is given by

$$T(\Delta_A, N) = T_0(\Delta_A) \left| \frac{\tilde{\Delta}_A + i\Gamma'/2}{\tilde{\Delta}_A + i\Gamma'/2 + (J_{1D}^{(N)} + i\Gamma_{1D}^{(N)}/2)} \right|^2, \quad (\text{S5})$$

where $\tilde{\Delta}_A = 2\pi\Delta_A = 2\pi(\nu_p - \nu_{D1})$ is the detuning between the pump and the atomic frequency, and $T_0(\Delta_A)$ is the device transmission when no atoms are present.

Explicitly accounting for the atoms’ positions by substituting Eq. (S4) into Eq. (S5), the transmission is given by

$$T(\Delta_A, N; x_1, \dots, x_N) = T_0(\Delta_A) \left| \frac{\Delta'_A + i\Gamma'/2}{\Delta'_A + i\Gamma'/2 + \sum_{j=1}^N (J_{1D} + i\Gamma_{1D}/2) \cos^2(x_j \pi/a)} \right|^2. \quad (\text{S6})$$

We have defined $\Delta'_A \equiv \tilde{\Delta}_A + \Delta_0$ in order to account for AC Stark shift Δ_0 of the atoms due to the dipole trap.

In order to accurately model the experimental conditions, we average the transmission model over atom positions and atom number. During a single measurement, the atoms are free to move along the length of the device, evenly sampling the Bloch function. We let $\langle T(\Delta_A, N; x_1, \dots, x_N) \rangle_x$ be an average over all positions, i.e.,

$$\langle T(\Delta_A, N; x_1, \dots, x_N) \rangle_x = T_0(\Delta_A) \int_0^a dx_1 \dots dx_N \left| \frac{\Delta'_A + i\Gamma'/2}{\Delta'_A + i\Gamma'/2 + \sum_{j=1}^N (J_{1D} + i\Gamma_{1D}/2) \cos^2(x_j \pi/a)} \right|^2. \quad (\text{S7})$$

We repeat the measurement tens of times for each frequency Δ_A . Each experiment can have a different number of atoms, and so we average the transmission expression over a Poisson distribution $P_{\bar{N}}(N)$, which is a function of the average atom number \bar{N} . The transmission model averaged over both atom positions and atom numbers is given by

$$\langle T(\Delta_A, N; x_1, \dots, x_N) \rangle_{x,N} = T_0(\Delta_A) \sum_N P_{\bar{N}}(N) \langle T(\Delta_A, N; x_1, \dots, x_N) \rangle_x. \quad (\text{S8})$$

This is the final form of the transmission model that we use to fit the atomic spectra.

Assuming $\bar{N} = 3.0$, which is obtained from the atom decay rate measurement, we fit the TE atomic spectra with Eq. (S8) and extract Γ_{1D} , J_{1D} , Γ' , and Δ_0 for each frequency. We show the values of Γ_{1D} and J_{1D} in Fig. 4(a) of the main text. We show the AC Stark shift and non-guided decay rate in Fig. S5.

The average of the non-guided decay rate Γ' for the TE data outside the bandgap is $\Gamma' = 2\pi \times 9.1$ MHz. This is significantly larger than the expected value from the FDTD simulation, $\Gamma' = 2\pi \times 5.0$ MHz. This additional inhomogeneous broadening is likely due to either the finite temperature of the trapped atoms, any residual components of circular light in the SI beam, atom density dependent collisional broadening, or any stray magnetic field. We estimate the contributions individually, finding that they may not each explain the full part of the broadening. We note that the estimation in temperature of trapped atoms could be improved in the future [S6], and it may help shed light on our excess broadening.

Interestingly, the fitted Γ' increases in the bandgap, and is as high as $\Gamma' = 2\pi \times 16$ MHz for the last measured point. One possible explanation is that this is due to the break-down of the single bright mode approximation, as coupling to multiple collective atomic modes should result in a broadened linewidth.

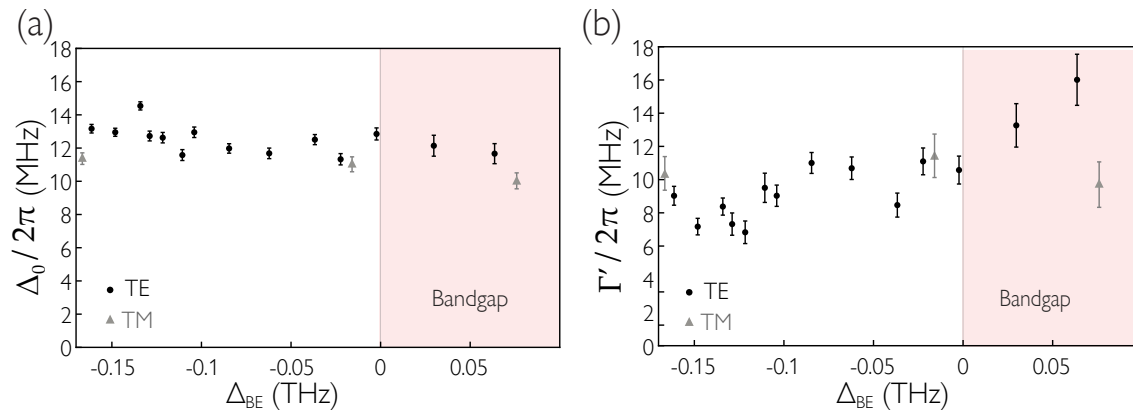


FIG. S5: Fitted values from averaged transmission model for TE (black, circles) and TM (gray, triangles) spectra. **(a)** Fitted AC Stark shift Δ_0 . **(b)** Fitted Γ' .

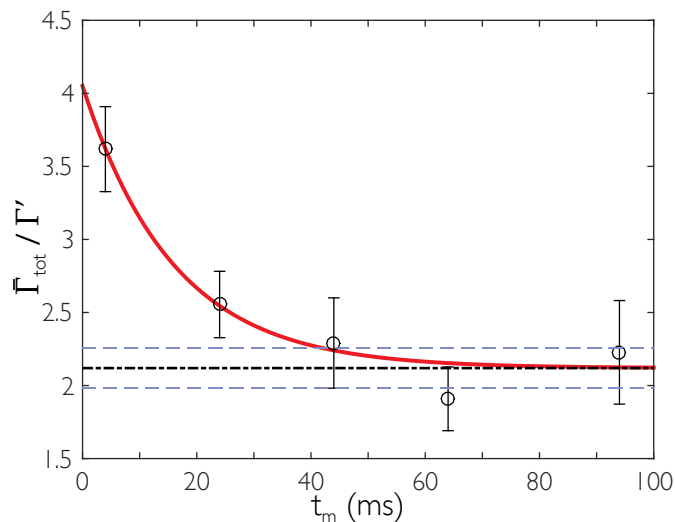


FIG. S6: Total decay rates as a function of holding time t_m . The red solid curve is the empirical fit and the dash-dot line represents the fitted asymptotic total decay rate at very long times. The blue dashed lines specify fitted error boundaries. The fit yields $\tau_{SR} = 16$ ms, $\bar{\Gamma}_{SR} = 1.5\Gamma'$ and the asymptote $\bar{\Gamma}_{tot}^{(1)}/\Gamma' = 2.12 \pm 0.14$.

We also measure transmission spectra for the TM mode, whose band edges are far-detuned from the Cs transitions.

The transmission in this waveguide regime is described by an optical density model

$$T/T_0 = \exp \left[\frac{-\text{OD}}{1 + \left(\frac{2\Delta'_A}{\Gamma_{1D}^{\text{TM}} + \Gamma'} \right)^2} \right], \quad (\text{S9})$$

where the resonant optical density is given by $\text{OD} = 2\bar{N}\Gamma_{1D}^{\text{TM}}/\tilde{\Gamma}'$. We fit the TM spectra with this model and extract Γ' , Δ_0 , and (assuming $\bar{N} = 3$) Γ_{1D}^{TM} . The values of Γ' and Δ_0 are shown with the TE data in Fig. S5. The averaged Γ_{1D}^{TM} value is $0.044 \Gamma_0$, which is ~ 30 times smaller than Γ_{1D} for the TE mode at the first resonance ν_1 , and clearly demonstrates the enhanced interaction due to the PCW.

ATOM DECAY MEASUREMENT

We exploit the superradiance of atoms trapped near the alligator APCW to determine the mean atom number \bar{N} and the peak atom decay rate Γ_{1D} (at ν_1) into the guided-modes.

As established in Ref. [S4], the total exponential decay rates of atoms is $\bar{\Gamma}_{\text{tot}} = \bar{\Gamma}_{\text{SR}}(\bar{N}) + \bar{\Gamma}_{\text{tot}}^{(1)}$, where $\bar{\Gamma}_{\text{SR}}$ is the \bar{N} -dependent superradiance decay rate, and $\bar{\Gamma}_{\text{tot}}^{(1)}$ is the observed single-atom decay rate. We note that when $\bar{N} \ll 1$, $\bar{\Gamma}_{\text{tot}} \sim \bar{\Gamma}_{\text{tot}}^{(1)} = \bar{\Gamma}_{1D} + \Gamma'$, as the superradiance effect diminishes and only the single-atom decay rate into GM $\bar{\Gamma}_{1D}$ and into environment Γ' remain. Γ' is numerically calculated to be $2\pi \times 5.0$ MHz for cesium D_1 line at the trapping site near the APCW [S4].

We probe the atoms with a weak resonant light pulse through the guided-mode, while the first resonance ν_1 near the band edge is aligned with cesium D_1 line. The subsequent fluorescence decay rates $\bar{\Gamma}_{\text{tot}}$ are determined through exponential fits. By varying the trap holding time t_m after loading, we adjust the atom numbers for the measurement. The decay rates are empirically fitted in an exponential form as a function of holding time t_m [S4]: $\bar{\Gamma}_{\text{tot}}(t_m) = \bar{\Gamma}_{\text{SR}}e^{-t_m/\tau_{\text{SR}}} + \bar{\Gamma}_{\text{tot}}^{(1)}$, as shown in Fig. S6. From the fitted asymptotic-value of the decay rates, we deduce that the apparent single-atom decay rate is $\bar{\Gamma}_{1D} = (1.12 \pm 0.14)\Gamma'$.

Because the atoms are randomly distributed along x direction in the trap, the observed decay curves are results after spatial averaging the coupling rates $\Gamma_{1D}(x)$. Assuming an uniform distribution of N atoms around the center of the APCW, a more detailed model specifies the form of fluorescence intensity decay as [S4]:

$$\mathcal{I}_N(t) = \gamma^2 e^{-(N\gamma + \Gamma')t} \cdot I_0(\gamma t)^{N-2} \cdot \left[\frac{N(N+1)}{4} I_0(\gamma t)^2 - \left(\frac{N}{4\gamma t} + \frac{N^2}{2} \right) I_0(\gamma t) I_1(\gamma t) + \frac{N(N-1)}{4} I_1(\gamma t)^2 \right], \quad (\text{S10})$$

where $\gamma = \Gamma_{1D}/2$, and I_k is the modified Bessel function. Numerically simulating the decay of single atoms in the trap by using $\mathcal{I}_1(t)$, we compare between the exponentially fitted value $\bar{\Gamma}_{1D}$ and the value of Γ_{1D} used for $\mathcal{I}_1(t)$, which yields a ratio of $\bar{\Gamma}_{1D}/\Gamma_{1D} = 0.81$. This is consistent with the ratio of 0.8 ± 0.3 from measurement at long hold time $t_m = 94$ ms, when single-atom decay predominates (shown as the asymptote in Fig. S6). Based on the values of $\bar{\Gamma}_{1D}$ deduced above, we conclude that $\Gamma_{1D} = (1.4 \pm 0.2)\Gamma'$.

At early holding times, the atom number N noticeably fluctuates around some mean values $\bar{N} \gtrsim 1$. To capture this \bar{N} -dependent variation, we fit the decay curves by averaging $\mathcal{I}_N(t)$ with weight function of Poisson distribution probability $P_{\bar{N}}(N)$ [S4]. The fitting parameter here is \bar{N} , while we fix the value of Γ_{1D} in Eq. S10. The fit is consistent with $\bar{N} = 3.0 \pm 0.5$ at $t_m = 4$ ms when we carry out the transmission spectra measurement. Based on the trap life time $\tau = 30$ ms, we further deduce that $\bar{N} \sim 0.1$ at $t_m = 94$ ms.

The linear \bar{N} -dependence of superradiance is given by $\bar{\Gamma}_{\text{SR}} = \eta \cdot \bar{N} \cdot \Gamma_{1D}$, where $\eta = 0.36 \pm 0.06$ is some linear coefficient, whose value is consistent with that reported in Ref. [S4].

[S1] Yu SP et al. (2014) Nanowire photonic crystal waveguides for single-atom trapping and strong light-matter interactions. *App. Phys. Lett.* 104:111103.

[S2] Lumerical Solutions, Inc., <http://www.lumerical.com/tcad-products/fdtd/>.

[S3] Hood JD et al (2016), in preparation.

- [S4] Goban A et al. (2015) Superradiance for atoms trapped along a photonic crystal waveguide. *Phys. Rev. Lett.* 115:063601.
- [S5] Dung HT, Knöll L, Welsch DG (2002) Resonant dipole-dipole interaction in the presence of dispersing and absorbing surroundings. *Phys. Rev. A* 66:063810.
- [S6] Tuchendler C, Lance AM, Browaeys A, Sortais YRP, Grangier P (2008) Energy distribution and cooling of a single atom in an optical tweezer. *Physical Review A* 78(3):033425.